Microscopy AND
Microanalysis

Original Article

Electron Beam Effects on Oxide Thin Films—Structure and Electrical Property Correlations

Krishna Kanth Neelisetty[1,2], Xiaoke Mu[1], Sebastian Gutsch[3], Alexander Vahl[4], Alan Molinari[1], Falk von Seggern[1], Mirko Hansen[5], Torsten Scherer[1,6], Margit Zacharias[3], Lorenz Kienle[4], VS Kiran Chakravadhanula[1,7,†] and Christian Kübel[1,6,7]*

[1]Institute of Nanotechnology, Karlsruhe Institute of Technology, 76344, Eggenstein-Leopoldshafen, Germany; [2]Technische Universität Darmstadt, 64289 Darmstadt, Germany; [3]Institute of Microsystems Engineering, Albert-Ludwigs-University Freiburg, 79110 Freiburg, Germany; [4]Institut für Materialwissenschaft, Technische Fakultät der CAU Kiel, 24143 Kiel, Germany; [5]Institut für Elektrotechnik, Technische Fakultät der CAU Kiel, 24143 Kiel, Germany; [6]Karlsruhe Nano-Micro Facility, Karlsruhe Institute of Technology, 76344, Eggenstein-Leopoldshafen, Germany and [7]Helmholtz Institute Ulm, Karlsruhe Institute of Technology, 76344, Eggenstein-Leopoldshafen, Germany

Abstract

In situ transmission electron microscope (TEM) characterization techniques provide valuable information on structure–property correlations to understand the behavior of materials at the nanoscale. However, understanding nanoscale structures and their interaction with the electron beam is pivotal for the reliable interpretation of *in situ/ex situ* TEM studies. Here, we report that oxides commonly used in nanoelectronic applications, such as transistor gate oxides or memristive devices, are prone to electron beam induced damage that causes small structural changes even under very low dose conditions, eventually changing their electrical properties as examined via *in situ* measurements. In this work, silicon, titanium, and niobium oxide thin films are used for *in situ* TEM electrical characterization studies. The electron beam induced reduction of the oxides turns these insulators into conductors. The conductivity change is reversible by exposure to air, supporting the idea of electron beam reduction of oxides as primary damage mechanism. Through these measurements we propose a limit for the critical dose to be considered for *in situ* scanning electron microscopy and TEM characterization studies.

Key words: dose, electrical properties, electron beam effects, *in situ* TEM, memristors, thin film oxides

(Received 16 November 2018; revised 25 December 2018; accepted 18 January 2019)

Introduction

Disordered dielectric metal and semiconductor oxide thin films are of great technological importance for a wide range of electronic applications, especially in the semiconductor industry (Kingon et al., 2000; Fortunato et al., 2012; Edwards et al., 2015; Yu et al., 2016), as gate oxides in transistors (Robertson, 2006) or tunnel barriers in non-volatile memories (Garcia Ruiz et al., 2009). A broad understanding and careful characterization of these devices at the nanoscale is of particular importance for further technological advances (Fortunato et al., 2012). Due to continued device miniaturization, advanced characterization tools such as high-resolution and *in situ* transmission electron microscopy (TEM) techniques are essential and well established to understand the structure–property correlations (Rudneva et al., 2013; Kamaladasa et al., 2014).

Recently, new types of electrical memories have been investigated, such as memristors (Kim et al., 2012a, 2012b; Zahari et al., 2015), to allow binary or analog switching behavior (Strukov et al., 2008). Redox-based memristors typically work on the principle of valence state change, where migration of anions and vacancies result in local redox reactions creating pathways for higher conductivity (low resistive state) and vice versa for lower conductivity (high resistive state). In both cases, the matrix for cation and vacancy migration is typically a thin film oxide (Edwards et al., 2015; Ielmini, 2016; Zidan et al., 2017; Wang et al., 2018). Experimentally demanding work has been conducted to understand the structure, processes and dynamics of memristive materials, and devices down to the atomic scale (Ha & Ramanathan, 2011; Yao et al., 2012; Fan et al., 2013; Park et al., 2013; Gale, 2014; Strobel et al., 2017). One of the critical issues in these studies is the complex data interpretation and evaluation to understand bulk materials/device properties from the local observations. One of the challenges involves sample preparation (Mayer et al., 2007; Langford & Rogers, 2008). For example, Ga implantation and defect generation during focused ion beam (FIB) sample preparation (Frey et al., 2003) and contamination during Pt, W, or C deposition (Hammad Fawey et al., 2016), as well as redeposition (Cairney & Munroe, 2003) cannot be completely avoided. Furthermore, surface effects, e.g. due to differences in diffusion properties can play a critical role, as well as the interaction with and damage by the electron beam (Aitken et al., 1978; Berger et al., 1987;

Egerton et al., 2004) during TEM characterization, leading, for example, to the generation of oxygen deficient structures (Egerton et al., 2010). While these effects are often quite well understood for *ex situ* analysis, *in situ* studies are more sensitive as the effects of these artifacts on the processes and physical properties are typically not well established. Depending on the properties of interest, small structural changes induced by the electron beam can potentially alter reaction pathways or properties of the materials/devices.

Electron beam damage is well known to be critical in *in situ* battery studies due to the sensitive lithium compounds (Lin et al., 2014; Mehdi et al., 2015) and the organic electrolytes (Drummy et al., 2004), even though the detailed effects on the reaction pathways during electrochemical cycling are often not established. In case of metal oxides or semiconductor oxides, electron beam damage is typically only considered to be a significant factor for TEM analysis at very high dose. This is partially because the structural changes due to the electron beam are often difficult to identify clearly, especially in amorphous oxides. However, the electrical response can be drastic, even at fairly low dose, for both low and high voltage scanning electron microscopy (SEM) and TEM. In this paper, we attempt to identify the changes in semiconductor and metal oxide systems during electron beam irradiation and correlate them with the electrical changes. We will discuss the electron beam induced damage using SiO_2, TiO_2, and Nb_xO_y as examples to study the damage mechanism, the structural changes induced and, in particular, the effect on the electrical properties. These results will be put in perspective with regard to *in situ* SEM/TEM measurements involving these oxides. The results of these studies can be applied to a wide range of applications, where typical oxide materials are studied and patterned by means of the electron beam—e.g. for electron beam lithographic techniques.

Methods and Materials

TEM analysis was performed using an aberration (image) corrected Titan 80-300 microscope (FEI Company, Portland, OR, USA) equipped with a US1000 slow scan CCD camera and a Tridiem 863 image filter (Gatan Inc., Pleasanton, CA, USA). The microscope was operated at 300 kV for beam damage studies. Energy filtered TEM (EFTEM) analysis was performed using a 5 eV energy slit centered on an energy loss of 17 eV to image the silicon distribution (Iacona et al., 2004) in the silicon oxide films. The electron dose rate was calculated from unfiltered TEM images, without a sample, with 1 s exposure time, acquired using the same illumination settings and camera, utilizing the calibrated conversion rate of counts to electrons of the camera.

The real space damage analysis of SiO_2 was performed using 20 nm silicon oxide windows (SO100 A20Q33A, Simpore, West Henrietta, NY, USA) as test object, applying a dose rate of 1.76×10^4 e/nm^2 s.

For the electron beam damage dependent conductivity measurements, a parallel electron beam illumination in TEM mode was used with a defined electron beam diameter of 36 or 16 μm. Dose rates of 670 and 1,100 e/nm^2 s were applied for SiO_2 and 1,100 e/nm^2 s in the case of NbO$_2$. As TiO_2 is more sensitive to the beam, it was exposed to a lower dose rate of 45 e/nm^2 s. The oxide thin films were directly deposited on MEMS-based electrical devices for the *in situ* measurements (E-AEK11, Protochips Inc., Morrisville, NC, USA) using various deposition methods:

(1) ~15 nm silicon oxide was deposited by plasma enhanced chemical vapor deposition (PECVD) (Hartel et al., 2011),

(2) ~15 nm silicon oxide was deposited by DC reactive magnetron sputtering (Supporting data—Experimental),

(3) ~30 nm titanium oxide was deposited by pulsed laser deposition, and

(4) ~30 nm niobium oxide was deposited by magnetron sputtering (Strobel et al., 2017). The stoichiometry of the films was determined by X-ray photoelectron spectroscopy (XPS) (Supporting information—XPS results).

A FUSION 200 electrical holder (Protochips Inc., Morrisville, NC, USA) with a Keithley 2636A SourceMeter (Tektronix Inc., Beaverton, OR, USA) and a Reference 600 potentiostat (Gamry Instruments, Warminster, PA, USA) was used for electrical measurements. A schematic of the chip and the electron beam exposed area is shown in Figure 2e. Voltage controlled I/V cycles were acquired over ±3 V with a scan speed of 66 mV/s. The electron beam was always turned off during the measurement to prevent the electron beam current contributing to the I/V curve (as an exception, the graphs in Supplementary Fig. S7 show the electron beam effect on the I/V measurement for TiO_2 and Nb_xO_y). In the case of silicon oxide, the first I/V curve was neglected as charging effects of the sample contribute to the first I/V curve. The second and third I/V curves are quite similar suggesting that all electron beam induced charging has been removed. The I/V curves and values shown in this paper for silicon oxide are always from the third I/V curve.

Low-voltage measurements were performed in a SEM using an Auriga 60 (Carl Zeiss AG, Oberkochen, Germany) dual beam FIB. A Faraday cup was used to measure the electron beam current at different operation voltages between 2 and 30 kV for various spot sizes to determine the dose rate and total dose. The conductivity measurements were performed using the same samples as previously in the TEM.

Results and Discussion

Electron Beam Irradiation of Silicon Oxide

The electron beam induced damage in silicon oxide is interesting because it is one of the most established oxides for microelectronic applications. Similar to previous work (Gutsch et al., 2015), EFTEM dose series, acquired on pure SiO_2 thin films (TEMwindows, West Henrietta, NY, USA) at an energy loss of 17 eV, reveal the continuous formation of silicon-rich mostly disordered particles with increasing dose (Fig. 1) due to an electron beam induced reduction of the silicon oxide film. Initially, at 300 kV and a dose of up to 1.9×10^6 e/nm^2 with a dose rate of ~1.76×10^4 e/nm^2 s no silicon nanoparticles are visible in the EFTEM images of the film, only a slight cloudy appearance can be noticed. With increasing dose, particles start to segregate visibly, and both the number and average size of these particles increase with dose. Hence, the distance between the particles is reduced considerably, forming a close (perhaps interconnected) network of particles at a dose of ~8.5×10^6 e/nm^2. A further increase in dose eventually led to film degradation, to formation of holes, and finally breakage of the film. This is illustrated in Figure 1 for operation at 300 kV; similar damage was also observed at 80 kV (Gutsch et al., 2015). In order to understand the electron beam induced structural changes in silicon oxide, radial distribution functions (RDFs) by selected area electron diffraction (SAED) are recorded. The short-range order of the pristine amorphous SiO_2 thin film indicates that the as-prepared amorphous sample is similar to the structure in quartz. A distinctive peak in line with the Si–Si bond length in Si–diamond appears after dose of 3.7×10^7 e/nm^2.
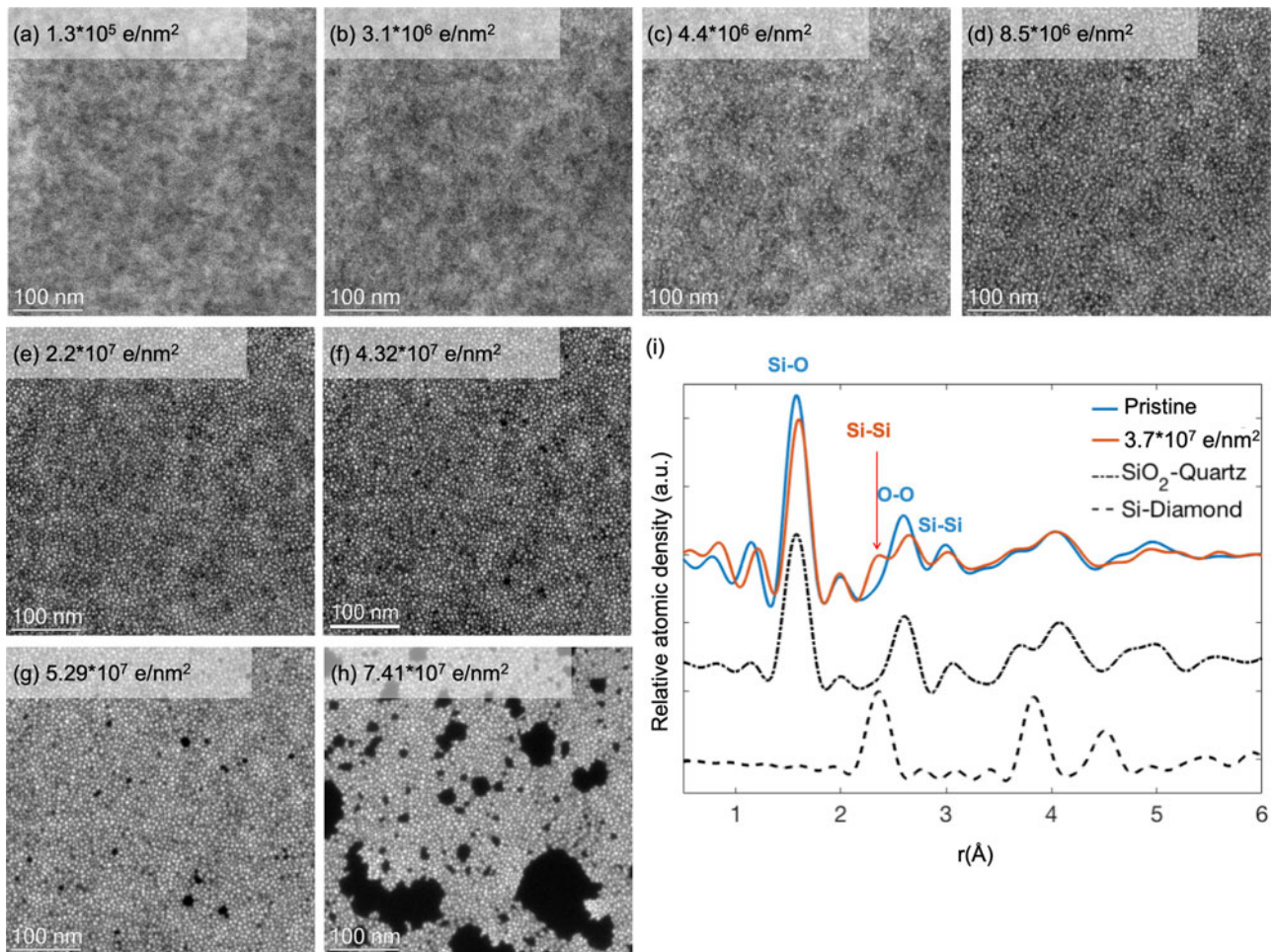
Fig. 1. EFTEM (at 17 eV energy loss) dose series showing Si nanoparticle formation under the electron beam. The dose rate was ~1.76×10^4 e/nm² s; the total dose is shown as inset in the images (**a–h**). (i) RDF analysis of the pristine silicon oxide film (blue curve) and beam induced damaged film after a dose of 3.7×10^7 e/nm² (red curve) with calculated RDFs (black) for crystalline SiO_2–quartz (dot dash curve) and crystalline Si–diamond (dash curve).

In addition, the reduced peak intensities corresponding to the Si–O and O–O distances compared to the pristine state shows that the sample is oxygen deficient. These observations indicate the reduction of the SiO_2 phase and an increase of the Si phase in the exposed area. In agreement with the EFTEM analysis, this confirms that the bright particles are a Si-rich phase with direct Si–Si bonding.

### Insulator to Semiconductor Transition

The silicon nanoparticles produced by the electron beam irradiation within the oxide (Fig. 1) resemble the silicon nanoparticle arrays investigated as active layer for silicon-based LEDs (Zacharias et al., 2002; Heitmann et al., 2003). The conductivity of the material would be expected to increase, when a dense non-connected network has formed enabling electrical transport by tunneling between particles and increase further when an inter-connected network is formed by electron beam reduction.

We investigated the electrical properties of the electron beam irradiated silicon oxides by measuring *in situ* dose dependent *I/V* curves as described in the experimental section for PECVD deposited SiO_2 thin films. Figures 2a to 2d show the effect of the electron beam and the structural changes induced on the conductivity of the silicon oxide film. Initially (Fig. 2a), the *I/V* curve

displays the typical shape of a capacitor, thus indicating that the as-prepared SiO_2 thin film behaves as an insulator. After electron beam exposure with a total dose of ~3×10^7 e/nm², the *I/V* curve (Fig. 2b) shows a significant increase in conductivity. This change in conductivity is related to the electron beam induced reduction of the film (charging effects due to the electron beam have been excluded). Considering the dose, we assume that the change in conductivity is related to the formation of a dense or even fully connected network of silicon particles within the oxide film. The resulting Si nanoparticle network significantly increases the electron mobility in the film. Due to the absence of dopants in the material, charge carriers have to be injected into the film from the contacts. Therefore, the conductivity is limited by the resulting space-charge that opposes the applied electric field.

The insulator to semiconductor behavior is reversible. When the sample is exposed to air, the electrical characteristics change back to a capacitive behavior (Fig. 2c). We assume that such reversibility is based on a partial re-oxidation of the silicon particles/network within the thin film in air causing a deterioration of the connected network and hence a low conductivity of the film. Subsequent electron beam exposure switches the behavior back to a semiconducting state (Fig. 2d). This switching between capacitive and conductive behavior by exposure to the electron beam
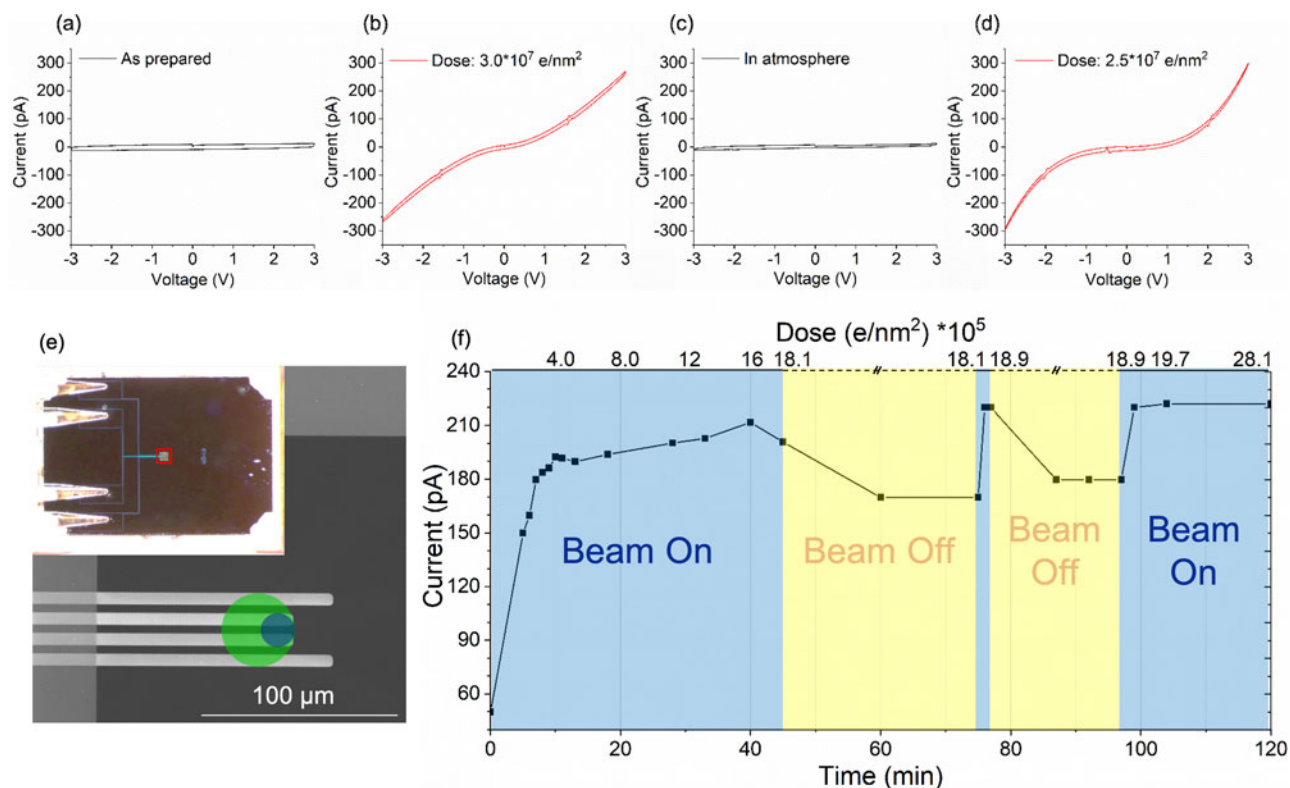
Fig. 2. *I/V* measurement on PECVD deposited SiO$_2$: transformation from insulating (**a**) to conductive (**b**) after electron beam exposure (dose ~3 × 10^7 e/nm^2), back to insulator (**c**) after exposure to atmosphere and finally back to conductive (**d**) after further electron beam exposure (dose 2.5 × 10^7 e/nm^2). Dose rate: ~670 e/nm^2 s. **e:** Schematic of the electrical chip. The green circle shows the area (*D* = 36 *μm*) exposed by the electron beam for SiO$_2$ and the blue circle (*D* = 16 *μm*) for titanium and niobium oxides for conductivity measurements. **f:** Electron beam induced conductivity changes and oxygen sensitivity of PECVD deposited SiO$_2$: current measured at 3 V depending on dose and reoxidation time in the TEM.

and air can be repeated extensively for both the PECVD and the magnetron sputtered silicon oxide films (data not shown). Interestingly, during the second (or further) electron beam exposure, a much lower dose is sufficient to achieve the switching compared to the first cycle. We tried to image the differences between the exposed and reoxidized state by EFTEM (Fig. S4). However, imaging the broken network turned out to be difficult, as the dose for the second electron beam reduction is much less than the minimum dose required to record an EFTEM image at sufficient resolution and signal to noise to detect the particles (see critical dose for conductivity changes of a pre-irradiated sample later).

Electron Dose Dependence

The evolution from insulator to semiconductor was examined in more detail for the magnetron sputtered SiO$_2$ thin film (Fig. 3a). Initially, the film was insulating, resulting in a capacitive element in our setup prior the electron beam exposure (black *I/V* curve). With increasing dose, the evolution from a capacitive to a semiconductive behavior can be seen clearly. The corresponding evolution of the maximum current at 3 V is plotted in Figure 3b. The plot clearly shows that during the early stages of electron beam exposure, up to a dose of ~4.8 × 10^7 e/nm^2, essentially no conductivity change is observed. Afterward, first a slight increase in the
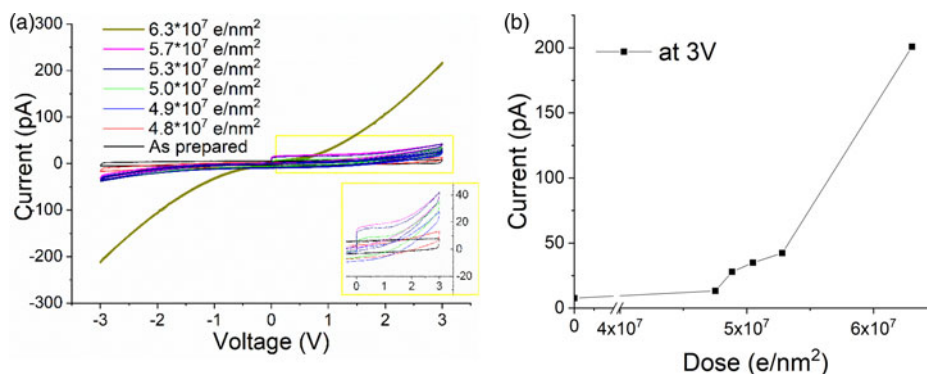
Fig. 3. a: *I/V* cycles showing the evolution of a magnetron sputtered SiO$_2$ from capacitive to a conductive state. Dose rate 1,100 e/nm^2 s. **b:** Electron beam (300 kV) induced conductivity changes: dose versus current at 3 V.

conductivity, and then at 6.3×10^7 e/nm^2, a significant increase is observed. This general behavior would fit the silicon particle evolution presented before: during an incubation time, no significant conductivity change is observed until the silicon particle network is dense enough to enable charge transport by tunneling. Once an interpenetrating network is formed, the conductivity should increase significantly again.

The absolute dose measured for the increase in conductivity roughly fits the dose needed for significant nanoparticle formation as imaged by EFTEM (cf. Fig. 1g). However, the exact numbers do not match perfectly. This might be partially due to slight differences between the films (thickness, free standing versus SiN-supported, deposition conditions). However, probably more significant are dose rate and the experimental time during the study: as discussed in the beginning, reoxidation of the films leads to a recovery of the capacitive behavior. This reoxidation also occurs within the vacuum system of the TEM, due to the residual oxygen pressure in the TEM column and results in competing reduction and oxidation effects causing strong dose rate sensitivity. Unfortunately, it was experimentally not possible to use comparable dose rates for EFTEM imaging (1.76×10^4 e/nm^2 s) and the conductivity measurements (6.7×10^2 e/nm^2 s) because of the different illuminated areas for both measurements.

Reoxidation within the TEM column was investigated using one of the PECVD grown SiO$_2$ thin films. Figure 2f shows the evolution of the maximum current at 3 V with respect to time and dose during the third electron irradiation cycle (the corresponding I/V plots are shown in Supplementary Fig. S5). The initial conductivity is a bit higher than in the as-prepared state, suggesting that the film had not fully recovered from the previous electron beam exposure prior to this experiment. After the third electron beam exposure was started, the maximum current quickly increased and asymptotically approached a maximum value of ~210 pA after around 40 min of exposure at a dose rate of 670 e/nm^2 s. When the electron beam was turned off for 30 min, the maximum current decreased by ~20%. A brief exposure to the electron beam results in a recovery of the maximum current and when the beam was turned off again, a decrease in the conductivity was observed again. This suggests that the network is more or less fully formed after 40 min during the third cycle and reoxidation without the electron beam leads to the

observed reduction of the conductivity, just much slower compared to exposure to air.

An important point is that already after 5 min beam exposure, corresponding to a dose of 2×10^5 e/nm^2, the current increased by 100 pA compared to the starting point of the third cycle. This dose is significantly lower compared to the 3×10^7 e/nm^2 required to initially observe an increased conductivity during the first cycle of this experiment (Figs. 2a–2d). This large difference of the dose required during initial and later electron beam illumination is because the sample does not reoxidize completely, but just enough to destroy the interconnected silicon network. Therefore, already a low dose is causing sufficient reduction during the following illumination to recreate the silicon network.

Supplementary Figure S6a shows further details on the recovery of the capacitive state in atmosphere, illustrating the evolution of the maximum current with time in air. As soon as the sample is in air the maximum current at 3 V immediately drops from ~250 to 100 pA and slowly reduces further to a saturation condition after about 3 h. It does not reach the as-prepared condition (maximum current ~15 pA—capacitive state), even after 10 h, indicating some residual leakage current in the film due to incomplete reoxidation.

Figure 4 schematically shows the electron beam induced evolution of the SiO$_2$ thin film into a composite with silicon particles embedded and its recovery as deduced from the EFTEM imaging and the conductivity measurements. The electron beam irradiation of the SiO$_2$ thin film causes formation of silicon-rich nanoparticles in the irradiated area. Increasing dose increases the particle size and the density of particles drastically, thus reducing the distance between them. In turn, the connected particles change the electrical properties of the film from a capacitive to a semiconducting state. When the film is exposed to air, the surface of these particles is reoxidized, increasing their distance and thus destroying an interconnected silicon network. This transforms the material from a semiconductor back to an insulator. When the sample is exposed to the electron beam again, even at low dose, we observe a rapid change in the conductivity of the film.

This observed effect of the electron beam on the electrical properties of silicon oxide might also be related to an earlier work by Mačković et al., where a change from brittle fracture to ductile was reported in silicon oxide nanospheres (Mačković et al., 2016) and thin films (Mačković et al., 2017).
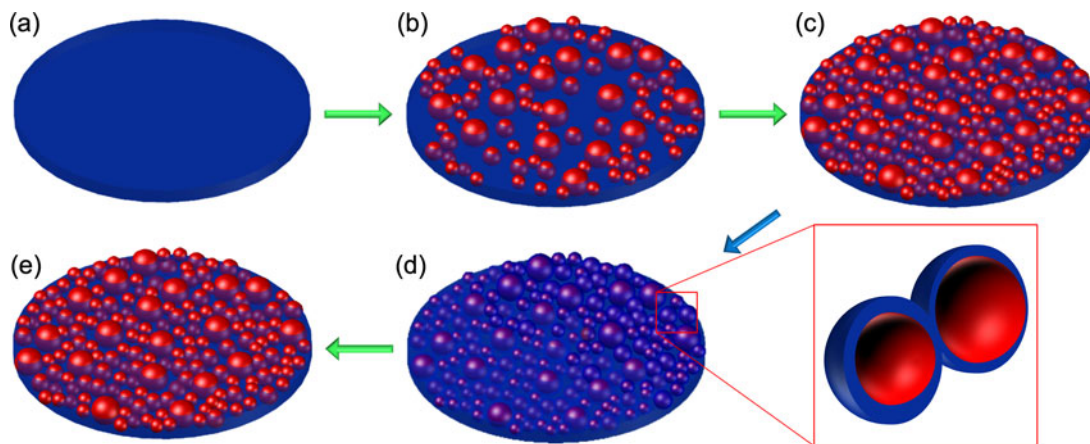
Fig. 4. Schematic illustration of the electron beam induced damage of the silicon oxide thin film leading to silicon particle formation in a composite with increasing dose (green arrow) (**a–c**) and resulting in an increased conductivity of the thin film. Once the sample is in atmosphere (blue arrow), a thin oxide layer forms on their surface (**d**) leading to the particles being disconnected from the network. Further exposure to the electron beam forms a connected network again (**e**) increasing the conductivity of the sample.

Comparing the electron beam sensitivity observed in our electrical measurements on SiO_2 ($\sim 5 \times 10^7$ e/nm²), and the changes observed in EFTEM ($\sim 2 \times 10^6$ e/nm²), with the electron beam sensitivity of organic materials such as pentacene or Cu-phthalocyanine ($\sim 10^4$–5×10^4 e/nm²) (Drummy et al., 2004), which are well known to be highly beam sensitive, the beam sensitivity at 300 kV is approaching that of small aromatic molecules and polymers.

The nucleation of Si nanoparticles in SiO_2 films irradiated by UV or soft-X-ray radiation has been reported to proceed via conversion of SiO_2 to SiO_x and oxygen desorption followed by disproportionation of SiO_x to Si and SiO_2 at elevated temperatures (Akazava, 2001), which could be compared to the mechanism for the electron beam induced formation and growth of silicon nanoparticles. Kumar et al. reported the densification of silica in SiO_2/HfO_2 multi-layers during neutron irradiation, which might be related to silicon particle formation, as well as void formation in SiO_2/Al_2O_3 multi-layers together with neutron induced silicon and aluminum diffusion within the multi-layers (Kiran Kumar et al., 2015). Changes of the electrical properties of quartz films due to heavy ion irradiation have been reported by Bush et al. and are discussed in terms of midgap interface states related to different trivalent silicon centers (Busch et al., 1992). MD simulations suggest the formation of more extensive structural damage leading to modification of the Si–O network and the formation of Si tetrahedra due to irradiation (Wang et al., 2015). While a direct comparison of these results with the damage in the amorphous silica thin films is not possible, the strong conductivity changes observed in our films are not related to individual defect centers as they only occur at a dose where a significant silicon nanoparticle density has been reached.
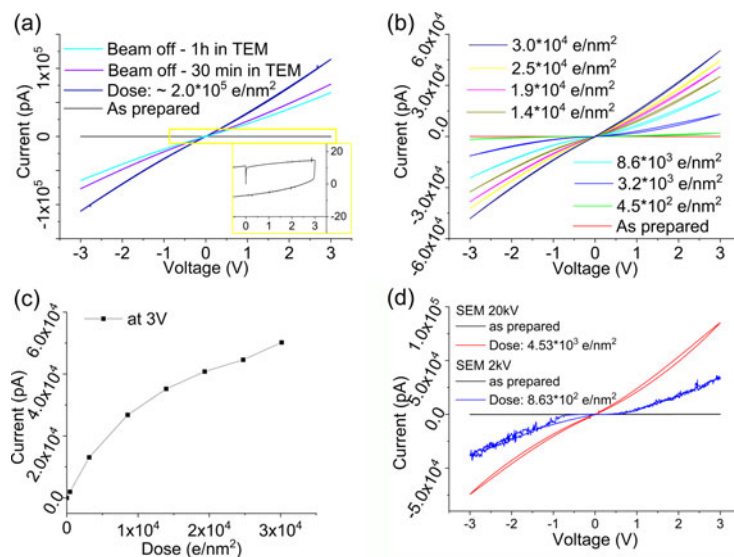
Electron Beam Damage of Titanium Oxide

Not only are silicon oxides sensitive to electron beam irradiation, but also metallic oxides. For example, for TiO_x Berger et al. have shown that the material changes at high current densities (Berger et al., 1987). Therefore, we used amorphous TiO_2 as another candidate to evaluate the electron beam sensitivity and its effect on the electrical properties. As it turned out, the electrical properties of TiO_2 are extremely beam sensitive even at very low dose. The I/V plots in Figure 5 show an insulating behavior of the TiO_2 thin film before exposure to the electron beam. At a dose of $\sim 2.0 \times 10^5$ e/nm² and a dose rate of 670 e/nm² s, we could identify the formation of a metallic material with the measured current being $\sim 1,000$ times higher compared to the irradiated semiconductor silicon oxide film. Similar to the silicon oxide case, the electron beam induced reduction is reversible upon reoxidation. This occurs instantaneously in air or slowly in the TEM because of the low oxygen partial pressure.

The electron beam induced evolution of the conductivity was studied in more detail using a low current density of 45 e/nm² s. Figure 5b shows the continuous increase in conductivity of the film with increasing dose. The first conductivity increase was detectable immediately after 10 s exposure at a dose as low as 4.5×10^2 e/nm². Thus, the electrical response of amorphous TiO_2 is around a factor of 1,000 more sensitive to the electron beam compared to SiO_2. The material generated at low dose shows an I/V curve characteristic of a semiconductor. Only at a higher dose of 3.0×10^4 e/nm², we see a transition to a metallic conductor.

Presumably, the transition from an insulator to a semiconductor and then to a metallic material upon electron beam exposure is related to reduction leading to the formation of TiO_{2-x} due to the progressive formation of oxygen vacancies. This electron beam reduction induced conductivity change is in line with the electrical properties of titanium suboxides reported by Bartholomew & Frankl (1969). The reason for the conductivity change being detected already at very low dose can be understood by the high sensitivity of the electrical conductivity on the oxygen content of TiO_{2-x} (Bartholomew & Frankl, 1969; Xu et al., 2016), with, for

Fig. 5. I/V curves recorded after electron beam exposure of titanium oxide thin films: (**a**) as-prepared film and after exposure to a total dose of 2.0×10^5 e/nm² resulting in a metallic conductivity; electron dose rate: 670 e/nm² s. After 30 and 60 min of the sample inside the TEM column (beam off), the conductivity is reduced considerably due to reoxidation; (**b**) I/V curves showing the evolution from a capacitive to a conductive state with increasing dose at a dose rate of 45 e/nm² s. **c:** Electron beam induced conductivity changes plotted as electron dose versus max. current at 3 V [from (**b**)]. **d:** I/V cycles showing the electron beam induced damage in a SEM of titanium oxide: as-prepared and after electron beam exposure at 20 kV—dose rate of 151 e/nm² s and at 2 kV—dose rate of 0.62 e/nm² s.

example, the magneli phases Ti_3O_5, Ti_4O_7, Ti_5O_9, and Ti_6O_{11} being reported as highly conductive. The conductivity difference of TiO_2 and Ti_4O_7 has also been discussed by Kwon et al. and these may be the active phases involved in switching states in TiO_2-based memristors (Kwon et al., 2010). Thus, the electrical response is different from the case of SiO_2 reduction, where first silicon-rich particles form and create an interconnected network, whereas in TiO_2 the reduction induced by creation of oxygen deficiencies is responsible for the electrical changes.

The RDF analysis of the amorphous TiO_2 thin film (Fig. S9) indicates that the short-range order of the pristine amorphous TiO_2 thin film reflects a mixture of rutile and anatase. However, we cannot differentiate between this anatase + rutile mixture and the sub-oxide phases as their short-range order is too similar. Therefore, we cannot unambiguously evaluate the structural changes during electron beam illumination.

In order to differentiate between ionization and knock-on damage as the main degradation mechanism in the titanium oxide thin films, we measured the electron beam induced conductivity dependence on the operation voltage. Figure 5d shows I/V curves recorded for the same titanium oxide samples as previously analyzed in the TEM, after electron beam irradiation in the SEM.

Beam damage of TiO_2 is also observed in the SEM at 20 kV with a dose rate of ~ 150 e/nm^2 s and at 2 kV with a dose rate of 0.6 e/nm^2 s. The transformation from an insulating state to a conductor is evident in the SEM similar to that seen in the TEM. This clearly confirms electron beam damage of the films at very low dose and very low voltage.

At 2 kV acceleration voltage, knock-on damage should not be a significant contribution, suggesting that ionization damage is critically contributing at this voltage. A true quantitative comparison of the damage is difficult because of the changing imaging conditions, dose rate and illuminated oxide area (about 2× larger in SEM compared to TEM). However, the measured current per dose and contact area is of the same order at 2, 20, and 300 kV, reduced by a factor of ~ 2–5 at 300 kV. If ionization was solely responsible for the damage at 300 kV, a stronger increase in electron beam stability should be observed between 20 and 300 kV (Egerton, 2012), indicating that at 300 kV, knock-on damage is also contributing to the damage of the sample. The influence of the electron beam on the electrical property measurements of TiO_2 is similar to imaging structural changes in typical aliphatic molecules and polymers, orders of magnitude more sensitive than e.g. graphene.
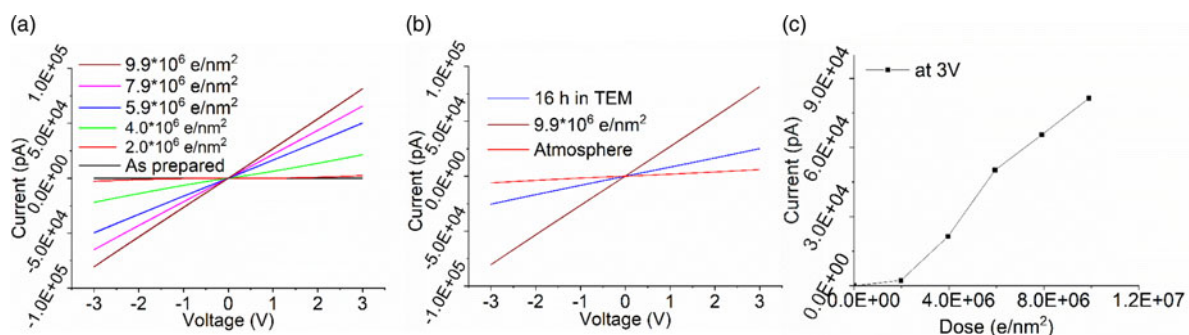
Niobium Oxide

Nb_xO_y is an insulating material in the as-prepared state, but also shows a conducting behavior after illumination with the electron beam. The dose required for the reduction is between that of SiO_2 and TiO_2. At a dose rate of 1,100 e/nm^2 s at 300 kV, the thin film was insulating up to a dose of 1×10^6 e/nm^2. Thereafter, niobium oxide showed a steady increase in conductivity (Fig. 6a). However, in contrast to titanium oxide, the I/V curves indicate metallic conductivity. No transition through a semiconducting behavior has been observed. Metallic conductivity has been reported for niobium suboxides (Bach, 2009). Similar to titanium oxide, niobium oxide seems to show a conductivity change by reduction to suboxides rather than reduction to particles as in silicon.

When the sample is kept in the high vacuum of the TEM column, reoxidation leading to a reduction of conductivity (Fig. 6b) is slower compared to the titanium oxide or silicon oxide films. Only in atmosphere, the conductivity of the film drops quickly returning to the insulating material.

Comparison of the Oxide Behavior

From the dose versus resistivity plots (Fig. S10) we define a critical dose in analogy to the use of electron diffraction data for beam sensitivity analysis to compare the three oxides. For a comparison of our results to the available electron beam sensitivity data from Egerton (2012), Drummy et al. (2004), Wang et al. (2009), and Meyer et al. (2008), Figure 7 shows the critical dose versus operating voltage for various materials. The black points represent the electron diffraction-based data from the literature. The blue points are the results obtained from the present electron beam induced conductivity studies. The green point in the plot corresponds to the first particles visible in the silicon oxide thin films by EFTEM imaging. While it is not possible to directly correlate diffraction and resistivity-based beam sensitivity measurements, it provides a basis to estimate when critical property changes are occurring in the material. The actual numbers will depend on how much structural change is needed to observe any conductivity changes. In SiO_2 very significant structural changes have to occur before the resistivity changes, which is reflected by the first silicon-rich particles appearing a long time before any resistivity changes can be measured. On the other hand, in titanium (and presumably in niobium) oxide already very small structural changes are sufficient to introduce very significant resistivity

Fig. 6. I/V curves of electron beam exposed niobium oxide. Dose rate 1,100 e/nm^2 s. **a:** Evolution of conductivity with increasing dose; (**b**) reoxidation leading to a slow reduction in conductivity without the beam in the TEM and fast after exposure to air; and (**c**) electron beam induced conductivity changes plotted as electron dose versus max. current at 3 V [from (**a**)].
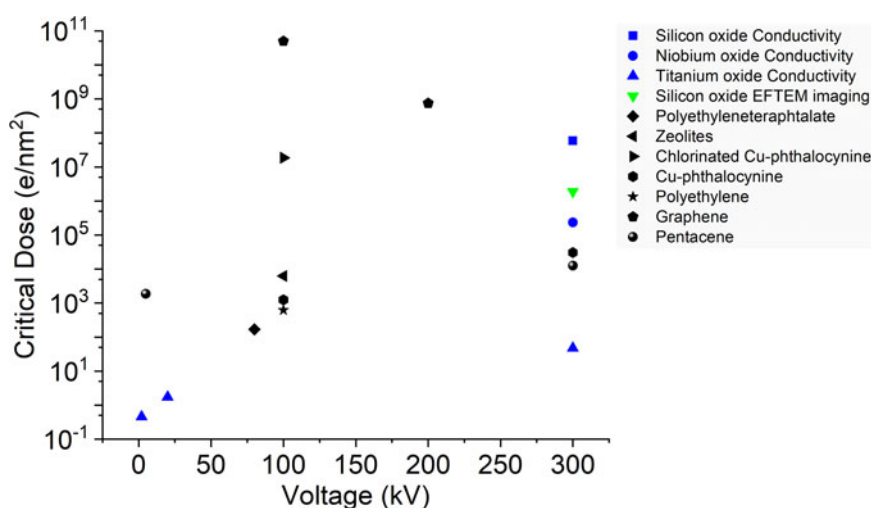
Fig. 7. Critical dose versus operating voltage for various materials (black) (Drummy et al., 2004; Meyer et al., 2008; Wang et al., 2009; Egerton, 2012) and the present results (colored).

changes, making the electrical measurements a very powerful tool to estimate damage. Overall, the critical dose we observe in these measurements are in the same range as for typical organic materials, indicating how crucial it is to consider electron beam effects during *in situ* TEM.

Conclusions

In this work, we show that even small amounts of structural damage caused by electron beam induced reduction at low dose can significantly alter the properties of amorphous oxide materials. Contrary to common experience, all three oxide films investigated in this work are prone to electron beam damage even at low doses, similar to organic materials.

Due to electron beam induced reduction, the electrical properties of SiO_2, TiO_2, and Nb_2O_5 thin films change from an insulating to a semiconducting or metallic state. The reversibility of the electron beam induced electrical properties by exposure to air is a strong indication that the damage mechanism is electron beam induced reduction of the oxides.

In SiO_2 the damage proceeds via formation of silicon-rich nanoparticles in the oxide matrix, which might interconnect to a penetrating network resulting in a conductivity change. In contrast, in TiO_2 and Nb_2O_5 the conductivity changes are directly related to the formation of suboxides, which are highly conductive. This is why the dose required for the conductivity change in silicon oxide is higher compared to the other two metal oxides. Based on the high electron beam sensitivity of TiO_2 at low voltages and a slightly reduced sensitivity at 300 kV, we assume that ionization damage is the most critical contribution, but knock-on damage might also add to the reduction at high voltages. As one approach to quantify this, we defined a critical dose for electron beam damage by looking at the resistivity changes of three oxides.

We speculate that these results can be extended to other oxide materials, which will also exhibit strong beam sensitivity and corresponding changes of the electrical properties. While the effects are not drastic for most classical *ex situ* SEM/TEM analysis, the conductivity changes have to be critically considered for any *in situ* SEM and TEM measurements. These experimental results prove that electron beam effects will significantly alter *in situ* electrical tests.

References

Aitken JM, Young DR & Pan K (1978). Electron trapping in electron-beam irradiated SiO_2. *J Appl Phys* **49**, 3386–3391.

Akazava H (2001). Formation of silicon nanocrystals and interface islands in synchrotron-radiation-irradiated SiO_2 films on Si(100). *Int J Mod Phys B* **15**, 3749–3752. Available at https://doi.org/10.1142/S0217979201008573.

Bach D (2009). EELS Investigations of Stoichiometric Niobium Oxides and Niobium-based Capacitors. 210. Available at http://en.scientificcommons.org/51213445.

Bartholomew RF & Frankl DR (1969). Electrical properties of some titanium oxides. *Phys Rev* **187**, 828–833.

Berger SD, Macaulay JM & Brown LM (1987). Radiation damage in TiOx at high current density. *Philos Mag Lett* **56**, 179–185.

Busch MC, Slaoui A, Siffert P, Dooryhee E & Toulemonde M (1992). Structural and electrical damage induced by high-energy heavy ions in SiO_2/Si structures structural and electrical in SiO_2/Si structures damage induced by high-energy heavy ions. *J Appl Phys* **71**, 2596. Available at https://doi.org/10.1063/1.351078.

Cairney JM & Munroe PR (2003). Redeposition effects in transmission electron microscope specimens of FeAl-WC composites prepared using a focused ion beam. *Micron* **34**, 97–107.

Drummy LF, Yang J & Martin DC (2004). Low-voltage electron microscopy of polymer and organic molecular thin films. *Ultramicroscopy* **99**, 247–256.

Edwards AH, Barnaby HJ, Campbell KA, Kozicki MN, Liu W & Marinella MJ (2015). Reconfigurable memristive device technologies. *Proc IEEE* **103**, 1004–1033.

Egerton RF (2012). Mechanisms of radiation damage in beam-sensitive specimens, for TEM accelerating voltages between 10 and 300 kV. *Microsc Res Tech* **75**, 1550–1556.

Egerton RF, Li P & Malac M (2004). Radiation damage in the TEM and SEM. *Micron* **35**, 399–409.

Egerton RF, McLeod R, Wang F & Malac M (2010). Basic questions related to electron-induced sputtering in the TEM. *Ultramicroscopy* **110**, 991–997. Available at http://dx.doi.org/10.1016/j.ultramic.2009.11.003.

Fan Z, Fan X, Li A & Dong L (2013). *In situ* forming, characterization, and transduction of nanowire memristors. *Nanoscale* **5**, 12310. Available at http://xlink.rsc.org/?DOI=c3nr03383j

Fortunato E, Barquinha P & Martins R (2012). Oxide semiconductor thin-film transistors: A review of recent advances. *Adv Mater* **24**, 2945–2986.

Frey L, Lehrer C & Ryssel H (2003). Nanoscale effects in focused ion beam processing. *Appl Phys A: Mater Sci Process* **76**, 1017–1023.

Gale E (2014). TiO_2-based memristors and ReRAM: Materials, mechanisms and models (a review). *Semicond Sci Technol* **29**, 104004.

Garcia Ruiz F, Tienda-Luna IM, Godoy A, Donetti L & Gamiz F (2009). Equivalent oxide thickness of trigate SOI MOSFETs with high-k insulators. *IEEE Trans Electron Devices* **56**, 2711–2719. Available at http://ieeexplore.ieee.org/lpdocs/epic03/wrapper.htm?arnumber=5263011.

Gutsch S, Hiller D, Laube J, Zacharias M & Kübel C (2015). Observing the morphology of single-layered embedded silicon nanocrystals by using temperature-stable TEM membranes. *Beilstein J Nanotechnol* **6**, 964–970. Available at http://www.beilstein-journals.org/bjnano/content/6/1/99.

Ha SD & Ramanathan S (2011). Adaptive oxide electronics: A review. *J Appl Phys* **110**, 071101.

Hammad Fawey M, Chakravadhanula VSK, Reddy MA, Rongeat C, Scherer T, Hahn H, Fichtner M & Kübel C (2016). *In situ* TEM studies of micron-sized all-solid-state fluoride ion batteries: Preparation, prospects, and challenges. *Microsc Res Tech* **79**, 615–624. Available at http://doi.wiley.com/10.1002/jemt.22675.

Hartel AM, Hiller D, Gutsch S, Löper P, Estradé S, Peiró F, Garrido B & Zacharias M (2011). Formation of size-controlled silicon nanocrystals in plasma enhanced chemical vapor deposition grown SiO_xN_y/SiO_2 superlattices. *Thin Solid Films* **520**, 121–125. Available at http://dx.doi.org/10.1016/j.tsf.2011.06.084.

Heitmann J, Schmidt M, Zacharias M, Timoshenko VY, Lisachenko MG & Kashkarov PK (2003). Fabrication and photoluminescence properties of erbium doped size-controlled silicon nanocrystals. *Mater Sci Eng, B* **105**, 214–220.

Iacona F, Bongiorno C, Spinella C, Boninelli S & Priolo F (2004). Formation and evolution of luminescent Si nanoclusters produced by thermal annealing of SiOx films. *J Appl Phys* **95**, 3723–3732.

Ielmini D (2016). Resistive switching memories based on metal oxides: Mechanisms, reliability and scaling. *Semicond Sci Technol* **31**, 063002.

Kamaladasa RJ, Sharma AA, Lai Y-T, Chen W, Salvador PA, Bain JA, Skowronski M & Picard YN (2014). *In situ* TEM imaging of defect dynamics under electrical bias in resistive switching rutile-TiO_2. *Microsc Microanal* **21**, 1–14. Available at http://journals.cambridge.org/abstract_S1431927614013555.

Kim H, Sah MP, Yang C, Cho S & Chua LO (2012a). Memristor emulator for memristor circuit applications. *IEEE Trans Circuits Syst Regul Pap* **59**, 2422–2431.

Kim KH, Gaba S, Wheeler D, Cruz-Albrecht JM, Hussain T, Srinivasa N & Lu W (2012b). A functional hybrid memristor crossbar-array/CMOS system for data storage and neuromorphic applications. *Nano Lett* **12**, 389–395.

Kingon AI, Maria J & Streiffer SK (2000). Alternative dielectrics to silicon dioxide for memory and logic devices. *Nature* **406**, 1032–1038.

Kiran Kumar N, Leonard KJ, Jellison GE & Snead LL (2015). High-dose neutron irradiation performance of dielectric mirrors. *Fusion Sci Technol* **67**(4), 771–783. Available at https://doi.org/10.13182/FST14-875.

Kwon D-H, Kim KM, Jang JH, Jeon JM, Lee MH, Kim GH, Li X-S, Park G-S, Lee B, Han S, Kim M & Hwang CS (2010). Atomic structure of conducting nanofilaments in TiO_2 resistive switching memory. *Nat Nanotechnol* **5**, 148–153. Available at http://dx.doi.org/10.1038/nnano.2009.456.

Langford RM & Rogers M (2008). *In situ* lift-out: Steps to improve yield and a comparison with other FIB TEM sample preparation techniques. *Micron* **39**, 1325–1330.

Lin F, Markus IM, Doeff MM & Xin HL (2014). Chemical and structural stability of lithium-ion battery electrode materials under electron beam. *Sci Rep* **4**, 5694.

Mačković M, Niekiel F, Wondraczek L, Bitzek E & Spiecker E (2016). *In situ* mechanical quenching of nanoscale silica spheres in the transmission electron microscope. *Scr Mater* **121**, 70–74.

Mačković M, Przybilla T, Dieker C, Herre P, Romeis S, Stara H, Schrenker N, Peukert W & Spiecker E (2017). A novel approach for preparation and *In situ* tensile testing of silica glass membranes in the transmission electron microscope. *Front Mater* **4**, 10. Available at http://journal.frontiersin.org/article/10.3389/fmats.2017.00010/full.

Mayer J, Giannuzzi LA, Kamino T & Michael J (2007). TEM sample preparation and damage. *MRS Bull* **32**, 400–407. Available at http://journals.cambridge.org/abstract_S0883769400007272.

Mehdi BL, Qian J, Nasybulin E, Park C, Welch DA, Faller R, Mehta H, Henderson WA, Xu W, Wang CM, Evans JE, Liu J, Zhang JG, Mueller KT & Browning ND (2015). Observation and quantification of nanoscale processes in lithium batteries by operando electrochemical (S) TEM. *Nano Lett* **15**, 2168–2173.

Meyer JC, Kisielowski C, Erin R, Rossell MD & Crommie MF (2008). Direct imaging of lattice atoms and topological defects in graphene membranes. *Nano Lett* **8**, 3582–3586.

Park G-S, Kim YB, Park SY, Li XS, Heo S, Lee M-J, Chang M, Kwon JH, Kim M, Chung U-I, Dittmann R, Waser R & Kim K (2013). *In situ* observation of filamentary conducting channels in an asymmetric Ta_2O_{5-x}/TaO_{-x} bilayer structure. *Nat Commun* **4**, 2382.

Robertson J (2006). High dielectric constant gate oxides for metal oxide Si transistors. *Rep Prog Phys* **69**, 327–396.

Rudneva M, Gao B, Prins F, Xu Q, van der Zant HSJ & Zandbergen HW (2013). *In situ* transmission electron microscopy imaging of electromigration in platinum nanowires. *Microsc Microanal* **19**(Suppl 5), 43–48.

Strobel J, Hansen M, Dirkmann S, Neelisetty KK, Ziegler M, Haberfehlner G, Popescu R, Kothleitner G, Chakravadhanula VSK, Kübel C, Kohlstedt H, Mussenbrock T & Kienle L (2017). In depth nano spectroscopic analysis on homogeneously switching double barrier memristive devices. *Journal of Applied Physics* **121**, 245307, 1–25.

Strukov DB, Snider GS, Stewart DR & Williams RS (2008). The missing memristor found. *Nature* **453**, 80–83.

Wang B, Yu Y, Pignatelli I, Sant G & Bauchy M (2015). Nature of radiation-induced defects in quartz. *J Chem Phys* **143**, 024505. Available at https://doi.org/10.1063/1.4926527.

Wang J, Botton GA, West MM & Hitchcock AP (2009). Quantitative evaluation of radiation damage to polyethylene terephthalate by soft X-rays and high-energy electrons. *J Phys Chem B* **113**, 1869–1876. Available at http://www.ncbi.nlm.nih.gov/pubmed/19175298.

Wang Z, Rao M, Midya R, Joshi S, Jiang H, Lin P, Song W, Asapu S, Zhuo Y, Li C, Wu H, Xia Q & Yang JJ (2018). Threshold switching of Ag or Cu in dielectrics: Materials, mechanism, and applications. *Adv Funct Mater* **28**, 1–19.

Xu B, Sohn HY, Mohassab Y & Lan Y (2016). Structures, preparation and applications of titanium suboxides. *RSC Adv* **6**, 79706–79722. Available at http://xlink.rsc.org/?DOI=C6RA14507H.

Yao J, Zhong L, Natelson D & Tour JM (2012). *In situ* imaging of the conducting filament in a silicon oxide resistive switch. *Sci Rep* **2**, 242. Available at http://www.nature.com/articles/srep00242.

Yu X, Marks TJ & Facchetti A (2016). Metal oxides for optoelectronic applications. *Nat Mater* **15**, 383–396. Available at http://dx.doi.org/10.1038/nmat4599.

Zacharias M, Heitmann J, Scholz R, Kahler U, Schmidt M & Bläsing J (2002). Size-controlled highly luminescent silicon nanocrystals: A SiO/SiO_2 superlattice approach. *Appl Phys Lett* **80**, 661–663. Available at http://aip.scitation.org/doi/10.1063/1.1433906.

Zahari F, Hansen M, Mussenbrock T, Ziegler M & Kohlstedt H (2015). Pattern recognition with TiO_x-based memristive devices. *AIMS Mater Sci* **2**, 203–216.

Zidan MA, Chen A, Indiveri G & Lu WD (2017). Memristive computing devices and applications. *J Electroceram* **39**, 4–20.